ROYAL SOCIETY OF CHEMISTRY

PAPER

Check for updates

Operando monitoring of gassing dynamics in lithium-ion batteries with optical fiber photothermal spectroscopy

Tianye Zheng, [iD] †[ab] Haihong Bao,†*[ab] Feifan Chen,†[ab] Jingwen Wu,[ab] Pengcheng Zhao,[ab] Hoi Lut Ho,[ab] Shoufei Gao,[c] Yingying Wang,[c] Jiaqiang Huang,[d] Leiting Zhang, [iD] [e] Steven T. Boles [iD] [f] and Wei Jin*[ab]

Gaseous molecules are inherent byproducts of (electro-)chemical reactions in lithium-ion battery cells during both formation cycles and long-term operation. While monitoring gas evolution can help understand battery chemistry and predict battery performance, the complex nature of gas dynamics makes conventional mass spectrometry approaches insufficient for real-time detection. Here, we present a radically different methodology for *operando* analysis of gas evolution in lithium-ion batteries using optical fiber photothermal spectroscopy. By placing an optical hollow-core fiber inside the battery cell, evolved gases can rapidly diffuse into the hollow core of the fiber, enabling photothermal spectroscopy which precisely and selectively quantifies their concentrations without altering the internal operation of the cell. This approach facilitates identification of individual gaseous species, thereby allowing for further clarification (electro-)chemical reaction pathways. Collectively, we show that the evolution paths of C_2H_4 and CO_2 are closely associated with the formation of the solid electrolyte interphase, the selection of electrolyte salts, and the inclusion of specific additives. Significantly, we confirm for the first time the spontaneous formation of CO_2, which occurs exclusively in the presence of $LiPF_6$ salt. Beyond the scope of batteries, the methodology presented here offers substantial potential for broader applications, particularly in characterizing electrocatalytic processes, providing unmatched precision, accuracy, and scalability compared to existing analytical techniques.

Broader context

With the wide spread of electric vehicles and stationary energy storage facilities, ensuring the sustainable production and safe operation of rechargeable batteries is of vital importance. A reliable diagnostic tool capable of real-time monitoring of battery cells would be highly beneficial for elucidating cell chemistry and optimizing cell performance. Here, we present a miniature gas sensor based on optical fiber photothermal spectroscopy for *operando* monitoring of gas evolution inside battery cells. The new technique enables highly selective gas detection and reveals comprehensive gassing dynamics, offering valuable insights into internal chemical processes. Importantly, the sensing platform presented in this work can be readily extended to monitor additional gas species or adapted for use in other electrochemical energy systems.

[a] *Department of Electrical and Electronic Engineering, The Hong Kong Polytechnic University, Hung Hom, Kowloon, Hong Kong.*
E-mail: darren.ty.zheng@connect.polyu.hk, haihong.bao@polyu.edu.hk, wei.jin@polyu.edu.hk
[b] *Photonics Research Institute, The Hong Kong Polytechnic University, Hung Hom, Kowloon, Hong Kong*
[c] *Institute of Photonics Technology, Jinan University, Guangzhou, China*
[d] *Sustainable Energy and Environment Thrust, The Hong Kong University of Science and Technology, Guangzhou, China*
[e] *Department of Chemistry–Ångström Laboratory, Uppsala University, Uppsala, Sweden*
[f] *Department of Energy and Process Engineering, Faculty of Engineering, Norwegian University of Science and Technology, Trondheim, Norway*
† Equal contributions.

Introduction

Lithium-ion batteries (LIBs) play an irreplaceable role in consumer electronics, and their recent success is clearly highlighted by the widespread adoption of electric vehicles (EVs), aiming for significant reductions in CO_2 emissions in the automotive sectors.[1,2] At the same time, efforts are also being made in other energy sectors such as power grid, aerospace, and robotics, to integrate LIBs with improved energy densities, cycle lives, and operational safety.[3] A critical aspect of LIB manufacturing involves the formation of a stable solid

electrolyte interphase (SEI), referring to the formation process, which is crucial for determining the initial Coulombic efficiency (ICE) and overall battery lifetime, as well as sustainability.[2] It has been revealed that SEI forms on the surface of negative electrodes *via* electrolyte (solvent and salt) decomposition during the formation process of battery cells.[4] Typically, these decomposition reactions are accompanied by the generation of various gaseous species, the analyses of which can shed light on the nature and quality of SEI, thus providing insights into their origins and (electro-)chemical dynamics. Moreover, battery incidents, such as swelling, smoking, and firing, pose significant safety risks. A common and signature incident mode is thermal runaway, which is marked by the rapid generation of gases and leads to cell-level pressure failures. Early detection of these gases can critically enhance safety measures, helping to mitigate battery incidents, prolong battery lifespan, and optimize battery recycling.[2,3,5] Real-time monitoring of gassing dynamics inside battery cells is therefore highly desired, but necessitates gas sensors with rapid response to ensure prompt detection, a high specificity to rule out undesirable gas interferences, and a compact size for seamless integration.

Meeting these requirements is challenging for existing technologies. Currently, in academia, *operando* studies of battery gassing dynamics predominantly rely on the differential/online electrochemical mass spectrometry (DEMS/OEMS), which involves flowing a carrier gas, such as argon or helium, through a battery cell to collect gases and transport them to a mass spectrometer for measurement. While DEMS/OEMS can be sensitive and versatile in quantifying various gaseous species, the equipment is generally cumbersome and may cause errors during the measurements. The system requires a specially designed cell connected to a gas flow channel, which modifies the internal environment of the cell. The introduction of a carrier gas can further alter the partial pressures of gases within the cell. For example, the solubility of CO_2 in organic carbonate-based electrolyte solutions may be affected by the partial pressures, thus hindering accurate measurements of CO_2.[6] Gas intermediates, such as PF_5 and POF_3,[7] may be stripped out from the cell before participating in further parasitic reactions. Additionally, a mass spectrometer identifies gas molecules by measurement of the mass-to-charge ratio *i.e.*, m/z, which suffers from insufficient specificity for gas detection with overlapped m/z signals (*e.g.*, C_2H_4, CO, and N_2).[8–10]

Optical fiber sensors have been demonstrated for *operando* measurements of temperature, strain, refractive index (RI), and gas pressure inside LIB cells.[5,11–13] These sensors offer advantages of compact structure, intrinsic safety, corrosion resistance, and immunity to electromagnetic interference without impacting the working conditions of LIBs. However, they do not capture key chemical indicators like gas species and concentrations, which are critical for comprehensive analyses of internal (electro-)chemical reactions. As motivated by these recent advancements, we propose employing hollow-core fiber (HCF) photothermal spectroscopy (PTS) sensors originally developed for atmospheric gas analysis for application in battery gas

sensing. Relying on the "fingerprint" molecular absorption line of gas molecules, the HCF–PTS sensors have exhibited excellent sensitivity and specificity.[14,15] Gas detection down to parts-per-million (ppm) or parts-per-billion (ppb) level can be achieved with a centimeter-long HCF, which could be conveniently embedded into a battery cell for *operando* gas measurements, therefore providing direct insights into internal (electro-)chemical reactions.[2,3,11–13]

Here, we report the use of an HCF–PTS sensor for real-time monitoring of the internal dynamics of the common cycling-related gaseous species: C_2H_4 and CO_2, to largely unlock the (electro-)chemical processes in early stages of LIB cell formation. For the first time, we place the micrometer–diameter HCF inside a battery cell, which requires only a minute amount of gas sample for sensing, ensuring fast response and unperturbed internal conditions of the battery cell during the measurement process. The HCF–PTS not only successfully captures the *operando* evolution of C_2H_4 with a high selectivity – an electrochemical process that is extensively documented in previous studies, but also enables the detection of a continues CO_2 formation – a purely chemical reaction step that has remained elusive with existing gas sensing technologies. Furthermore, the data collected using our HCF–PTS system is compared with those obtained from DEMS/OEMS systems in previous studies, offering a more comprehensive perspective on the internal chemistries and dynamic processes in LIBs, while paving a path for enhancing battery lifetime and sustainability.

Results

HCF–PTS for gas detection

Fig. 1a illustrates the structure of the optical fiber sensor, which is constructed by mechanically splicing a 5-cm-long HCF to two cleaved single-mode fibers (SMFs). The HCF has a silica outer cladding with an inner diameter of ~ 56 μm, seven capillary rings with a diameter of ~ 14 μm and a thickness of 370 nm, giving an inscribed air core with a diameter of 28 μm, as shown in Fig. 1a.[14] Gaps of a few hundred micrometers are kept at the HCF/SMF joints to facilitate gas exchange in and out of the hollow-core.

A pump laser beam (indicated as an orange arrow) with its wavelength tuned to a specific absorption line of a target gas is delivered into the sensing HCF through a SMF. The gas absorption of the modulated pump inside the HCF generates heating, which modulates the temperature and refractive index (RI) of the gas sample, and hence the phase of a probe beam (indicated as a blue arrow) propagating through the HCF. The photothermal (PT) phase modulation ($\Delta\varnothing$) of the probe beam is given by eqn (1):[14,15]

$$\Delta\varnothing \propto C_t \cdot \alpha(\lambda_{pump}) \cdot L \cdot P_{pump} \qquad (1)$$

where C_t is the concentration of the target gas, λ_{pump} is the pump wavelength, α is the gas absorption coefficient, L is the interaction length between light beams and gas molecules, P_{pump} is the average pump power over L. The HCF provides
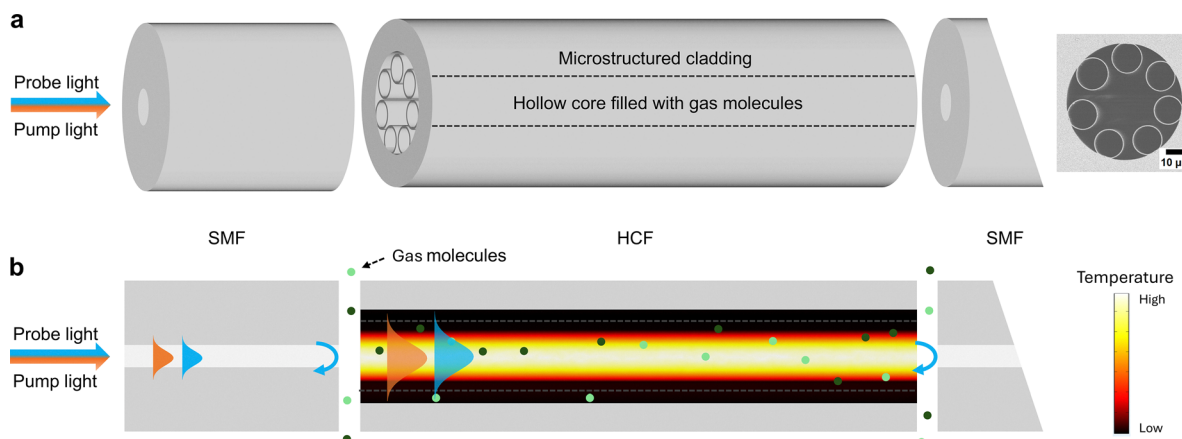
Fig. 1 The HCF−PTS gas sensor. (a) Schematic of the HCF gas sensor with the cross-sectional image provided on the righthand side. (b) The temperature (hence RI) profile over the HCF. The intensity profiles of the probe and pump beams and gas molecules are also superimposed onto the temperature profile. The angled end-face of the SMF eliminates the parasitic reflection.

an ideal platform to confine the gas molecules, the pump and the probe beam simultaneously in the hollow core at micrometer scale that enhances the PT phase modulation by orders of magnitude over an open-path gas cell per equal length.[15]

Among various fiber-based interferometric configurations developed for detecting the PT phase modulation,[14–16] we use the most compact one with the configuration shown in Fig. 1a. The reflections at the SMF-HCF joints forms a low-finesse Fabry–Pérot interferometer (FPI), which detects the phase difference between the reflected probe beams (Fig. 1b). Simultaneous detection of multiple gas species is achieved by using multiple pump lasers, each tuned to the selected absorption lines of the target gas species and modulated at distinct frequencies to generate respective phase modulations. This HCF–PTS gas sensor offers high sensitivity, selectivity, and a large range of measurements. The miniature and

electrical-insulating design makes it highly suitable for integration into battery cells.

HCF–PTS platform for *operando* dual-gas detection in LIB cells

Fig. 2a depicts the absorption lines of C_2H_4, CO_2, CH_4, CO, H_2 and O_2 based on data acquired from PNNL[17] and HITRAN[18] online databases. These gases are common byproducts produced during battery cycling.[19] Each of these gases exhibits distinct absorption features, which can be selectively targeted by choosing appropriate pump laser wavelengths. Here we selected C_2H_4 and CO_2 as the target gases and detected them near 1654.5 nm and 2004.0 nm, respectively. Fig. 2b and c provide the enlarged views of absorption for the two gases around 1654.5 nm and 2004.0 nm, which are well-separated and have minimal cross-interferences with other gases, allowing for highly unambiguous detection. In the case of
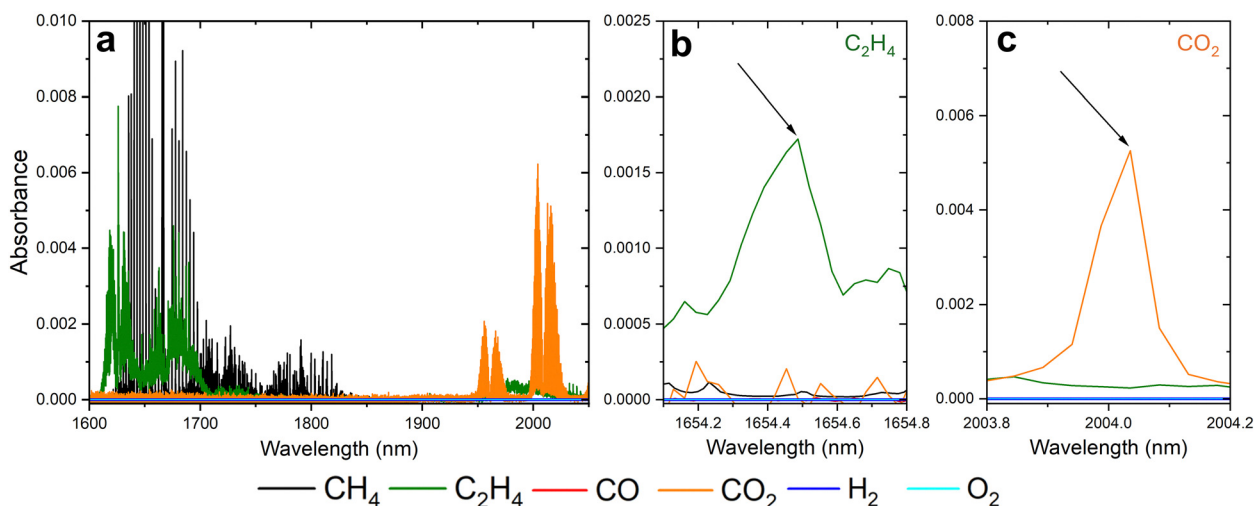

Fig. 2 Absorption lines of common gases produced during battery cycling. (a) Absorption lines of C_2H_4, CO_2, CH_4, CO, H_2 and O_2 based on the PNNL and HITRAN online database from 1600 nm to 2050 nm. (b) and (c) The target absorption lines for the detection of C_2H_4 and CO_2. The absorbance is calculated based on a 5-cm long HCF.

This journal is © The Royal Society of Chemistry 2025

Energy Environ. Sci., 2025, **18**, 8499–8514 | **8501**

overlapping absorption lines, a spectral fitting algorithm based on least-squares optimization can be used to minimize the measurement error.[20]

Schematically illustrated in Fig. 3, the gas detection system of HCF–PTS employs two distributed feedback (DFB) pump lasers with wavelengths tuned to the absorption lines of C_2H_4 near 1654.5 nm and CO_2 near 2004.0 nm. Two optical amplifiers, *i.e.*, a Raman fiber amplifier (RAF) and a thulium-doped fiber amplifier (TDFA), are employed to boost the pump power, thereby enhancing the PT-induced phase modulation and improving the measurement sensitivity. A probe beam from a fiber laser at 1550 nm is combined with the two pump beams using a wavelength-division multiplexer (WDM) and launched into the HCF sensor.

To achieve a higher signal-to-noise ratio (SNR), wavelength modulation and harmonic detection are employed. The pump laser wavelength is modulated sinusoidally at a high frequency and swept slowly across the gas absorption line. For optimal phase detection, the FPI is stabilized at its quadrature point with a servo controller using the DC component of the reflected probe beam detected by photodetector 1 (PD1).[21] The reflected probe beam is also detected by PD2 and its second harmonic (2f) signal, which is proportional to gas concentration, is demodulated by a lock-in amplifier (LIA). Frequency-division multiplexing (FDM) is employed to enable the simultaneous detection of multiple gases.[22] The two pump lasers are modulated at distinct frequencies, *i.e.*, 10 kHz for C_2H_4 and 8 kHz for

CO_2, allowing the 2f signals to be demodulated simultaneously at their corresponding second harmonic frequencies by the LIA. The time constant used in LIA is 400 ms with 18 dB/Oct slope and the scanning frequency of both pump wavelengths is 10 mHz.

The HCF sensor is packaged using a stainless steel (SS) tube and attached to a homemade cell *via* a Swagelok connector as shown in Fig. 3. The inner volume of the 5-cm-long HCF is $\sim 0.12~\mu L$, while the total volume of the battery cell is estimated to be ~ 1.4 mL, resulting in a minimal influence on the gas environment within the cell. To monitor the overall change of the gas pressure within the LIB cell during charge–discharge, a commercial piezoelectric pressure sensor is also incorporated. After installing the gas and pressure sensors, cyclic voltammetry (CV) measurements are conducted, and results indicate that the battery performance remains largely unaffected. Detailed data can be found in Note 2, SI. All measurements were conducted with the homemade cell placed in an environmental chamber maintained at a constant temperature of 35 °C.

Determining the gas concentration from HCF–PTS measurement

Based on the working principle, the PT phase modulation is dependent on the gas concentration, temperature, and pressure.[23] In this study, experiments are conducted using a sealed battery cell placed inside an environmental chamber and the temperature fluctuation is minimal (Note 3, SI). As a
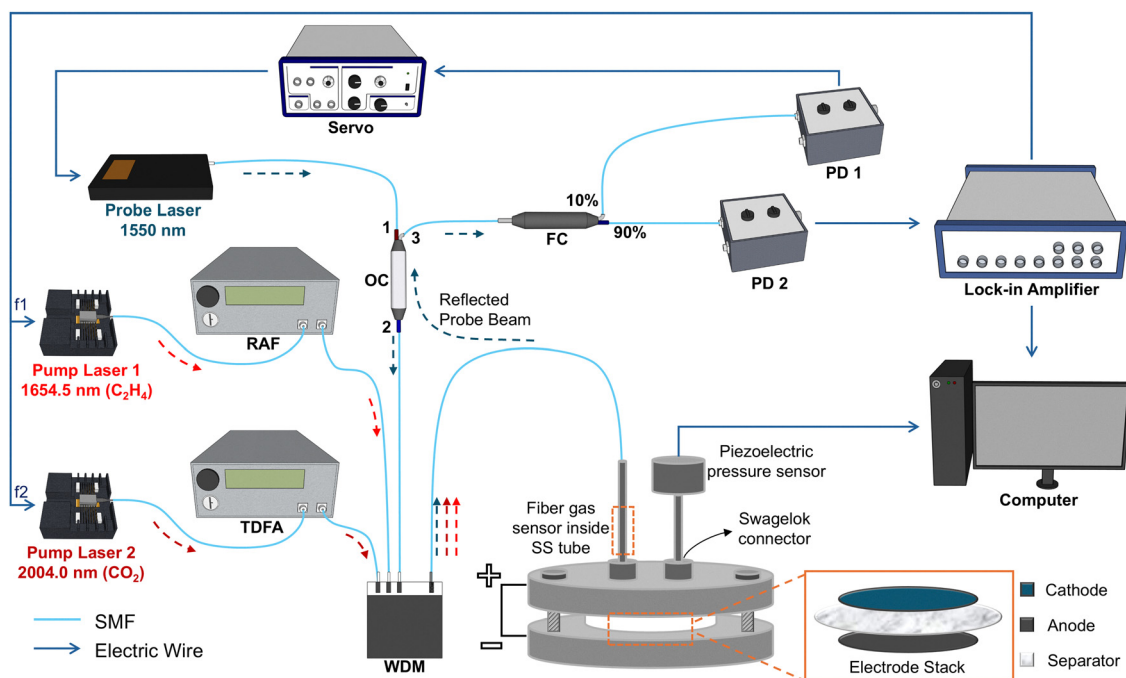

Fig. 3 HCF–PTS gas sensing platform for Li–ion cells. The experimental setup for simultaneous detection of C_2H_4 and CO_2. $f_1 = 10$ kHz and $f_2 = 8$ kHz are the modulation frequencies for pump laser 1 (for C_2H_4) and 2 (for CO_2). RFA: Raman fiber amplifier. TDFA: Thulium-doped fiber amplifier. OC: optical circulator. PD: photodetector. WDM: wavelength-division multiplexing. FC: fiber coupler. LIA: lock-in amplifier. A two-channel LIA is used for simultaneous detection of C_2H_4 and CO_2. The schematic of the homemade cell is also provided with the electrode stack being illustrated. Although the customized interrogation system in a lab scale may look bulky, it can be integrated into circuit boards to achieve the size of a desktop computer for application purposes. The digital images of the necessary components are supplied in Note 1, SI.

result, the primary variables affecting the amplitude of LIA output (S) are the target gas concentration (C_t) and the internal pressure (P) of the LIB cell. To accurately determine the target gas concentration, the HCF–PTS sensing system is firstly calibrated by introducing a reference gas sample with a known concentration C_r at an internal pressure P_r, producing a LIA output signal S_r. The concentration of the target gas is then calculated by using:

$$C_t = \frac{(S - S_r) - k_P \times (P - P_r)}{k_C} + C_r \qquad (2)$$

where k_C and k_P are the coefficients determined from calibration experiments, as detailed in Note 4, SI.

Additionally, it is necessary to characterize the performance of our HCF–PTS gas detection system in terms of response time and limit of detection (LOD) using standard gas samples under conditions of 35 °C and 1 atm. The response time of the HCF sensor, defined as the time required for the signal to rise from 0 to 90% of its maximum value (t_{90}),[14] is measured to be 14.5 seconds. The LOD is determined to be 2.5 ppm for C_2H_4 and 1 ppm for CO_2. Detailed determinations of response time and LOD are provided in Note 4, SI.

Demonstration of *operando* gas monitoring for battery cells

Initially, the HCF–PTS system is employed to monitor gas evolution inside a battery full cell assembled with commercial electrodes, *i.e.*, a LiFePO$_4$ (LFP) cathode and a graphite anode. As a starting point, a common commercial electrolyte blend is employed, consisting of 1 M of LiPF$_6$ salt dissolved in ethylene carbonate (EC) and ethyl-methyl carbonate (EMC) with 3 : 7 vol%. To minimize the influence of residue moisture, all cell components were subject to a rigorous drying process before being transferred to an argon-filled glovebox (Note 5, SI), and the electrolyte was freshly prepared and shipped to us by the supplier. The assembled cell then went through galvanostatic charge–discharge (GCD) cycles inside the environmental chamber, during which the gassing dynamics were recorded in real-time. As shown in Fig. 4a and b, the recorded gas signals from the LIA output are arranged in the 3-dimensional (3D) waterfall plots with the x-, y-, and z-axis denoting wavelength, LIA output, and time, respectively. The projections on the yz plane, *i.e.*, LIA output *vs.* time, reflect the concentrations of C_2H_4 and CO_2 evolved during cycling. We subsequently extract the peak-to-peak (p–p) values from these projections and quantify gas concentration (C_t) using eqn (2). Fig. 4c and d depict the evolution of concentrations of C_2H_4 and CO_2, respectively. The overall gas pressure change (P) is also monitored to provide insights into the other possible gassing events that may occur simultaneously.

The rates of change in the gas concentrations and pressure can then be determined by calculating their time derivatives, *i.e.*, dC/dt and dP/dt, aiming to shed light on the gassing events occurring at specific time points and/or electrode potentials. Fig. 4e presents the GCD profiles of the LFP-graphite full cell, along with the rates of change for overall pressure (dP/dt), as well as concentrations of C_2H_4 (d$C_{C_2H_4}$/dt) and CO_2 (dC_{CO_2}/dt).

From these results, the HCF–PTS system successfully captures well-documented gassing events, where the d$C_{C_2H_4}$/dt profile shows a gassing onset at a cell voltage of $\sim$2.8 V (equivalent to an anode potential of $\sim$0.6 V *vs.* Li/Li$^+$), about 20 minutes after the charging starts and reaches a peak formation rate at d$C_{C_2H_4}$/d$t \approx$ 6000 ppm h^{-1}. The C_2H_4 evolution stops at $\sim$3.3 V (equivalent to an anode potential of $\sim$0.1 V *vs.* Li/Li$^+$) and does not appear in the subsequent cycle, indicating that the selected initial charging rate should be sufficiently slow to form a passivating SEI layer on the graphite surface. During the initial charging of an LIB cell, C_2H_4 evolution is inevitable when EC is used as one of the electrolyte solvents, as it has been reported to originate exclusively from EC reduction with a lithium ethylene decarbonate (LEDC) intermediate electro-reduction product.[19,24,25] After the initial charging, the C_2H_4 concentration seems to decrease very slowly, from approximately 0.78% to 0.71% by the end of the second cycle (Fig. 4c). A similar trend is also observed in other studies using the OEMS technique.[26,27] Ellis *et al.* concluded that the C_2H_4 formed during the initial charging is gradually consumed at the cathode evidenced by an increase in cell impedance.[28] The small time-lag in the onset of the d$C_{C_2H_4}$/dt profile, compared to that in the dP/dt profile, can be attributed to the possible evolution of H$_2$, which likely originates from the reduction of protic electrolyte oxidation species (R–H$^+$) from the cathode.[26] Overall, the observed C_2H_4 dynamics correlate well with the dP/dt profile and are consistent with the previous studies,[24,26–28] affirming the validity of the measurements from the HCF–PTS system.

Beyond confirming previously reported C_2H_4 dynamics, our system also uncovers new and intriguing dynamics of CO_2 evolution: Before charging the LIB cell, the CO_2 concentration is non-zero and keeps increasing at a rate of dC_{CO_2}/d$t \approx$ 200–300 ppm h^{-1}. The non-zero level of CO_2 may partly originate from the background CO_2 in the glovebox, which was verified by a commercial electrochemical CO_2 sensor. The increase in CO_2 concentration before cycling suggests spontaneous CO_2-forming reactions without electrochemical driving forces. This spontaneous CO_2 formation is further confirmed by monitoring the gas evolution in the cell that only consists of the electrolyte and separator (Note 6, SI). Additionally, the airtightness of the homemade cell was double-checked to prove the claim (Note 7, SI). Once the battery charging begins, dC_{CO_2}/dt decreases significantly. When the cell voltage rises from 2.8 V to 3.3 V, the CO_2 concentration decreases with a maximum rate of dC_{CO_2}/d$t \approx$ −900 ppm h^{-1}. By integrating dC_{CO_2}/dt over time, the total decrease in CO_2 concentration is determined to be 1832 ppm as indicated by the shaded area below zero in the dC_{CO_2}/dt profile shown in Fig. 4e. As the cell voltage rises beyond 3.3 V, dC_{CO_2}/dt gradually restores to $\sim$200–300 ppm h^{-1} after the C_2H_4 evolution concludes. Notably, the dC_{CO_2}/dt profile remains stable and does not vary significantly during subsequent cycling, with the CO_2 evolution being independent of the cell voltage. Such spontaneous CO_2 formation in the absence of electrochemistry was not clearly acknowledged in previous studies using the DEMS/OEMS systems.[6,26,27,29,30] At the end of the second charge,
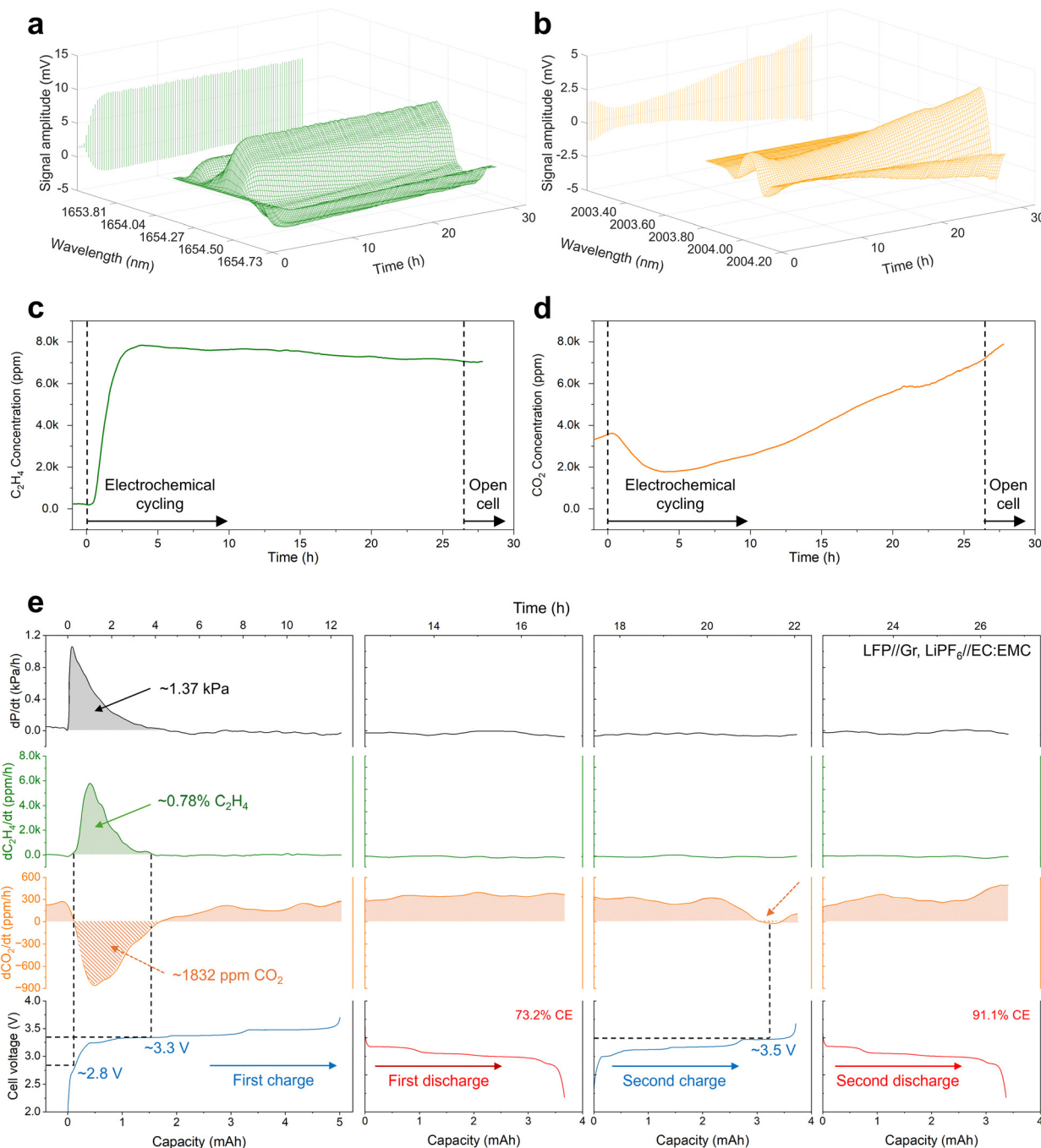
Fig. 4 *Operando* monitoring of gas evolution in LiFePO₄-graphite full cell with 1 M LiPF₆ in EC : EMC 3 : 7 vol% during the initial GCD cycles. (a) LIA output for C_2H_4 with the pump wavelength scanned from 1654.14 nm to 1654.73 nm. (b) LIA output for CO_2 with a pump wavelength scanned from 2003.81 nm to 2004.20 nm. The p–p values of the projections on the yz plane in (a) and (b) indicate the evolving concentrations for C_2H_4 and CO_2, which are then extracted and plotted in (c) and (d), respectively. (e) The GCD profile is plotted in conjunction with the change in concentrations of C_2H_4, CO_2, and in the overall gas pressure. A slow C-rate of ∼C/10 (0.402 mA) was used for the initial charge to allow a proper formation of SEI. The C-rate was then adjusted to ∼C/5 (0.804 mA) for the subsequent cycles.

a decrease in dC_{CO_2}/dt is observed as marked by a dashed arrow in the 3rd column of Fig. 4e when the cell voltage is above ∼3.5 V. Unlike the concentration decrease observed during the first charge, this decrease does not coincide with C_2H_4 generation, which suggests a different mechanism behind the

occurrence of CO_2 consumption, (re-)dissolution, or other gas-forming reactions that dilute the CO_2 concentration. Collectively, the newly revealed gassing dynamics from the classic Li-ion battery system merits further investigation and will be discussed in the following sections.

8504 | *Energy Environ. Sci.*, 2025, **18**, 8499–8514

This journal is © The Royal Society of Chemistry 2025

Characterization of graphite electrode in commercial LiPF$_6$ electrolytes

It is reported that the observed gas evolution in the LFP-graphite full cell is primarily attributed to the SEI formation on the surface of the graphite anode.[19,25] To confirm this conclusion, we replaced the graphite anode with a metallic Li foil. Interestingly, the evolution of C_2H_4 almost disappears after the anode replacement, while the seemingly spontaneous CO_2 formation largely persists (Note 8, SI). This suggests that the absence of C_2H_4 may be partly due to the significantly smaller specific surface area (SSA) of the metallic Li foil (~ 2 cm^2), compared to the composite graphite anode ($\varnothing$ = 12 mm) with an SSA ranging from 104.8 to 159.5 cm^2, which provides more available reaction sites for C_2H_4 evolution.[25,31] As a result, while the correlation between SSA and C_2H_4 evolution warrants further investigation, the Li-graphite half-cell can already serve as an ideal tool for studying the formation cycle and associated gas evolution of the graphite anode with minimized interference from the counter electrode. We carried out tests on half-cells using a slow CV scan at 0.05 mV s^{-1}, such that the system can precisely monitor the gassing events across different electrode potentials $vs.$ Li/Li$^+$. The tests were carried out with the LIB cell placed inside the same environmental chamber using the same electrolyte as before.

Fig. 5a presents the initial CV curve obtained from the Li-graphite cell alongside the evolution profiles of both C_2H_4 and CO_2 gases, as well as the overall gas pressure. Notably, the profile of $dC_{C_2H_4}/dt$ aligns well with the dP/dt, indicating a strong correlation between the C_2H_4 dynamics and the change in overall gas pressure. A distinct cathodic bump appears with an onset potential of ~ 0.9 V, peaking just below ~ 0.8 V $vs.$ Li/Li$^+$ as shown in the inset of the current–potential plot. This bump synchronizes with the increase of overall gas pressure and the initiation of C_2H_4 evolution results from the reduction of EC on the graphite electrode near ~ 0.8 V $vs.$ Li/Li$^+$.[26,27] In contrast, the dC_{CO_2}/dt profile shows that CO_2 concentration increases at a rate of approximately 200 ppm h^{-1} immediately after cell assembly. Interestingly, this spontaneous CO_2 formation does not significantly impact the overall gas pressure (≤ 0.1 kPa h^{-1}), suggesting that CO_2 solubility-vapor pressure dynamics are likely involved. As shown in Fig. 5b, the electrochemical impedance spectroscopy (EIS) measurements reveal no significant difference in cell impedance after the initial and the second cathodic scan, indicating the formation of a stable passivating SEI. Following the SEI formation, a pronounced increase in dC_{CO_2}/dt to 400 ppm h^{-1} is observed, during which no C_2H_4 generation or notable pressure variation occurs, suggesting that C_2H_4 and CO_2 evolution may be decoupled, with CO_2 also involved in other electrolyte decomposition reactions.[25]

Fig. 5c presents an alternative plot of gas concentration $vs.$ capacity for the initial cathodic scan, where the C_2H_4 concentration remains negligible until shooting up at nearly 0.1 mAh. Meanwhile, the CO_2 profile appears independent of capacity, suggesting that its formation is through spontaneous reaction

pathways. By integrating the cyclic voltammograms in the inset of Fig. 5a (blue shaded areas), we estimate the total electrons that are associated with the SEI formation until 0.3 V $vs.$ Li/Li$^+$ to be approximately 6.84 μmol (Note 9, SI). At this electrode potential, the intercalation of Li into graphite has not yet started. These electrons are irreversibly consumed in the formation of the SEI layer and the generation of gases, leading to an ICE of $\sim 86\%$. By applying the ideal gas law to the recorded pressure data, the change in total gas molecules within the cell is estimated to be ~ 0.64 μmol. Meanwhile, our HCF–PTS gas sensor quantifies the C_2H_4 molecules to be ~ 0.68 μmol through multiplying the concentration with the cell volume ($ca.$ 1.4 mL). These quantitative results confirm that C_2H_4 is the primary gas that evolved during SEI formation, playing a significant role in influencing overall cell pressure, aligning well with previous investigations.[24,28,29]

In contrast, CO_2 does not substantially influence the overall gas pressure. The high solubility of CO_2 in the electrolyte allows it to dynamically dissolve into or escape from the electrolyte, buffering changes in the overall gas pressure. Additionally, it is suggested that the CO_2 formation observed in Fig. 5a may be linked to the presence of LiPF$_6$. The LiPF$_6$ salt dissolved in the carbonate solvents can readily dissociate to form gaseous PF$_5$,[7,32,33] which is highly reactive with cyclic carbonate solvents, such as EC, triggering spontaneous CO_2 generation. This was evidenced by the observation that CO_2 generation is accompanied by a decrease of EC in an electrolyte of LiPF$_6$ in EC:DMC (dimethyl carbonate) at 85 °C.[34,35] Similarly, Ravdel et $al.$ employed both nuclear magnetic resonance (NMR) spectroscopy and gas chromatography-mass spectrometry (GC-MS) and observed that the dissociated PF$_5$ gas reacts with EMC, producing gaseous CO_2 and POF$_3$.[36] Further NMR studies indicate that POF$_3$ may cleave EC, resulting in the formation of CO_2 and OPF$_2$OCH$_2$CH$_2$F. This intermediate subsequently reacts with additional EC, further liberating CO_2 and forming capped oligoethylene oxides [OPF$_2$(OCH$_2$CH$_2$)$_n$F] by inserting ethylene oxide units into the P–O bond.[37] Our results suggest that these CO_2 formation reactions are largely independent of cell potential and are likely spontaneous and dependent on CO_2 presence itself. Scheme 1 summarizes the potential reaction pathways for spontaneous CO_2 formation, drawing on insights from prior studies.

The higher dC_{CO_2}/dt rate observed after the initial cathodic scan is perhaps caused by the decompositions of certain SEI components, such as Li$_2$CO$_3$, via LiPF$_6$ + Li$_2$CO$_3$ → CO_2(g) + 3LIF + POF$_3$(g).[19] Lithium methyl carbonate (LMC) may also thermally decompose to form CO_2 in the presence of LiPF$_6$ at 55 °C via LiPF$_6$ + 3LMC → 3CO$_2$(g) + 4LiF + OPF$_2$OCH$_3$ + CH$_3$OCH$_3$.[4] Parimalam et $al.$ found that adding LiPF$_6$ leads to the decompositions of certain SEI components during cell storage, resulting in the generation of a mixture of CO_2, LiF, ethers, phosphates, and (fluoro)phosphates. These results were confirmed by multiple experimental tools, including NMR, GC-MS, and infrared spectroscopy with attenuated total reflectance (IR-ATR).[4] Additionally, due to the difficulty in completely eliminating residual moisture from the electrodes
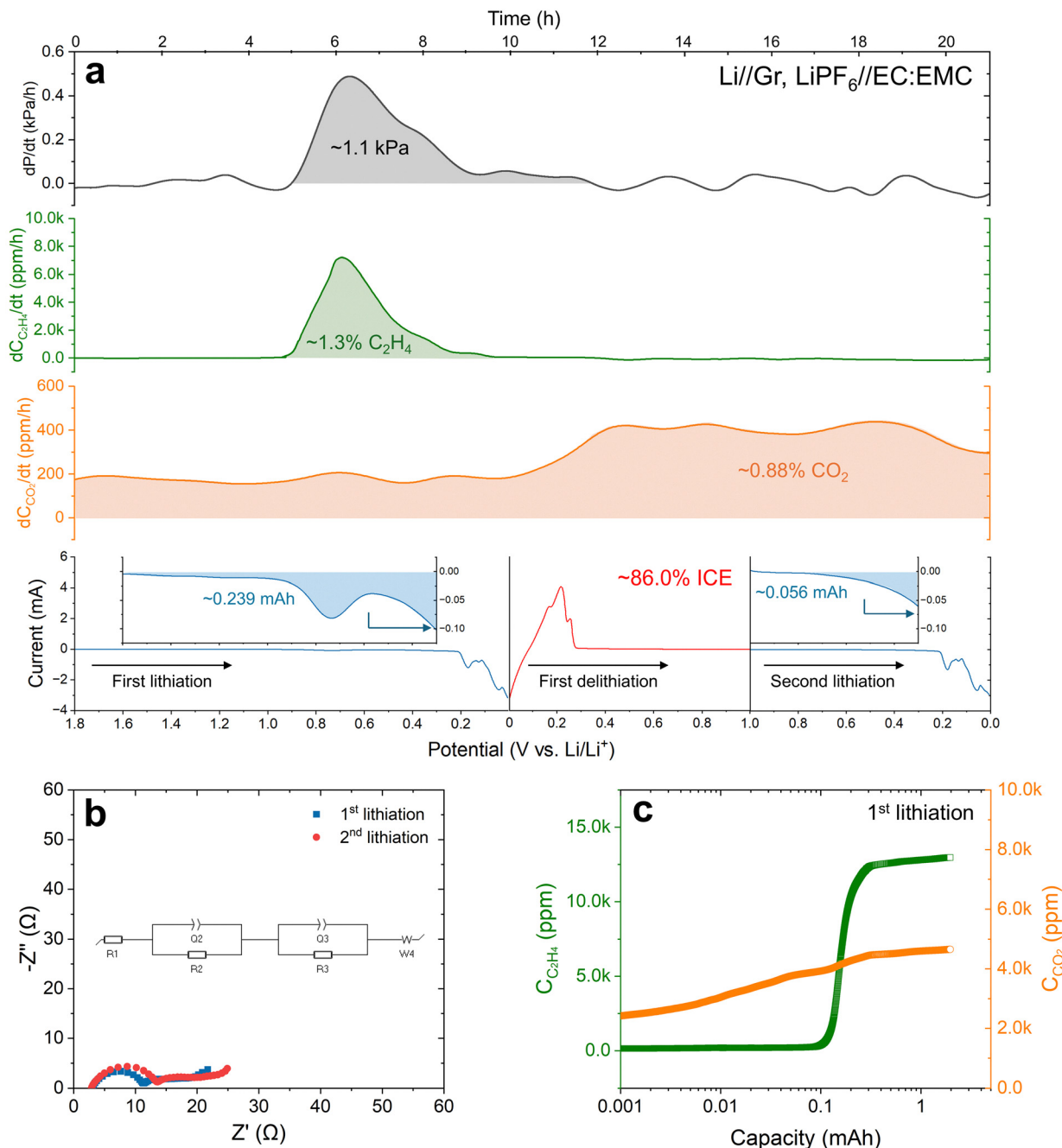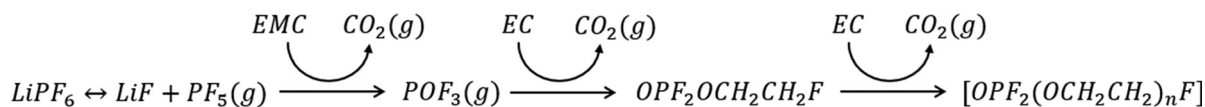
This journal is © The Royal Society of Chemistry 2025

Energy Environ. Sci., 2025, **18**, 8499–8514 | 8505

Fig. 5 *Operando* monitoring of gas evolution in the Li-graphite half-cell that undergoes cyclic voltammetry at a scan rate of 0.05 mV s⁻¹ with 1 M LiPF₆ in EC : EMC 3 : 7 vol% as the electrolyte. (a) The obtained CV curves are plotted in conjunction with the change in concentrations of C_2H_4, CO_2, and in overall gas pressure. The detailed current variation from 1.8 V to 0.3 V *vs.* Li/Li⁺ of the first lithiation and from 1 V to 0.3 V *vs.* Li/Li⁺ of the second lithiation is provided in the insets by zooming in the *y*-axis. The blue shading of the first lithiation represents the electric charge consumed for the SEI formation and associated gas evolution. (b) The EIS spectra obtained after the initial and the second cathodic scan. (c) Evolution of C_2H_4 and CO_2 concentrations during the initial lithiation of graphite.

Scheme 1 Suggested reaction pathways for the spontaneous CO_2 formation in LiPF₆//carbonate electrolytes.

and electrolytes, trace hydrofluoric acid (HF) may present in the $LiPF_6$-based electrolyte, which decomposes lithium alkyl carbonate to form CO_2 via $LiOCO_2CH_3 + HF \rightarrow LiF^+ + CH_3OH + CO_2$.[8]

According to literature, non-spontaneous (i.e., electrochemically-driven) CO_2 formation often occurs at the cathode surface with a high potential vs. Li/Li^+ due to oxidation of organic carbonate solvents via $RCO_3R \rightarrow ROR + CO_2(g)$.[8,38–40] When a cell is overcharged, the oxidation of conductive carbon and electrode binder may also lead to CO_2 formation.[29] However, neither of these cases seems to be occurring in the Li-graphite half-cell, where the electrode potential is relatively low. It is also reported that a 'water-contaminated' cell (~ 300 ppm H_2O) exhibits a more pronounced CO_2 evolution than a 'water-free' cell (≤ 20 ppm H_2O) when 1 M $LiPF_6$ in EC:DEC (diethyl carbonate) is used as the electrolyte.[6] An extra experiment was conducted to investigate the effect from water contamination, affirming and supporting that our drying process is sufficient. When the cell parts were not dried aggressively, the dC_{CO_2}/dt profile alters markedly with a notably higher level of CO_2 concentration (details in Note 10, SI).

Effect of electrolyte salts

To verify whether the observed spontaneous CO_2 formation originates from the presence of $LiPF_6$ salt, we replaced it with $LiClO_4$, keeping all other solvent ingredients unchanged, and repeated the same CV test. As shown in Fig. 6a, while the electrochemical behaviors and $dC_{C_2H_4}/dt$ profile are generally similar to those observed with the $LiPF_6$ salt (Fig. 5a), several key features after switching the electrolyte salt are highlighted: (1) the overall change of gas pressure is somewhat less pronounced; (2) the $dC_{C_2H_4}/dt$ profile remains largely the same; (3) the spontaneous CO_2 formation no longer occurs; (4) only minor changes are observed in electrochemical signals.

The insignificant change of the $dC_{C_2H_4}/dt$ profile upon replacing the electrolyte salt is consistent with the observation that C_2H_4 evolution results from the reduction of EC at the graphite electrode, which remains unchanged in both electrolytes. This claim is further supported by the EIS spectra in Fig. 6b, showing no noticeable change in cell impedance, thereby indicating similar electrochemical properties of the $LiClO_4$-derived SEI, which however does not contain inorganic species like LiF. The C_2H_4 dynamic shown in Fig. 6c is consistent with those of the cell using the $LiPF_6$-based electrolyte, though with a slightly shifted onset of increase of ≤ 0.1 mAh due to the elimination of the possible CO_2-producing reactions. Generally, this allows us to conclude that the series of reactions leading to C_2H_4 generation is PF_6^- independent, consistent with the EC-LEDC mediation discussed above.

Regarding CO_2 formation, while the precise reaction pathways can be quite complex, we provide strong evidence that its spontaneous formation originates from the presence of PF_6^-,[36,37] aligning well with the reaction pathways proposed in Scheme 1. In the $LiClO_4$-based electrolyte where PF_6^- is absent, no spontaneous CO_2 generation is detected either before or after the formation of SEI. Notably, CO_2 concentration decreases at the start of the CV scan. The total decrease in CO_2

concentration is determined to be 819 ppm by integrating dC_{CO_2}/dt over time as electrode potential decreases from 1.8 V to 1.0 V, suggesting that the background CO_2 in the glovebox may be dissolved into the carbonate electrolyte after cell assembly. Generally, this finding after replacing the electrolyte salt is consistent with a recent study by Lundström et al., who observed no clear sign of CO_2 evolution with $LiClO_4$ as the salt and EC as the solvent.[30]

The negligible level of dC_{CO_2}/dt during the second cathodic scan again underscores the role of $LiPF_6$ in facilitating the spontaneous CO_2 formation via both the electrolyte breakdown and SEI decomposition discussed above. While this $LiClO_4$-based electrolyte experiences less pressure change and negligible CO_2 production in the formation cycle, the presence of fluorine to passivate the aluminum-based cathode current collector mandates the use of $LiPF_6$-based electrolytes in commercial cells.

Effect of electrolyte solvents

It is a common practice to incorporate solvent additives, such as fluoroethylene carbonate (FEC) or vinylene carbonate (VC), into $LiPF_6$//carbonate electrolytes to promote the formation of a favorable SEI on the surface of negative electrodes.[41] We intentionally added 2 vol% of VC to the $LiPF_6$ in EC:EMC 3:7 vol% electrolyte and investigated the gas evolution by repeating the same experiment under the same conditions as described previously. The differences introduced by the VC additive are enumerated as follows: (1) the overall change in gas pressure becomes negligible; (2) the C_2H_4 concentration and its changing rate $dC_{C_2H_4}/dt$ are significantly reduced; (3) the (spontaneous) CO_2 formation becomes more pronounced; and (4) peak broadening of the electrochemical signal is observed during the first cathodic scan, accompanied by a decrease in ICE from $\sim 86.0\%$ to $\sim 79.6\%$.

In our experiment, the overall pressure change is too small to be detected by the commercial piezoelectric pressure sensor after adding VC. This is attributed to the more stable VC-derived SEI, which inhibits reduction reactions on the graphite anode surface and leads to less intensive gassing activity.[27] The results demonstrate that this minimal pressure change correlates with a significantly lower rate of $dC_{C_2H_4}/dt$, peaking at just above 1000 ppm h^{-1}, which is notably smaller than those shown in Fig. 5a and Fig. 6a. The significantly lower $dC_{C_2H_4}/dt$ in the presence of 2 vol% VC is attributed to the early reduction of VC at a relatively higher potential vs. Li/Li^+ than that of EC. While the exact onset potential for VC breakdown remains debatable, it is generally accepted to be above 1 V vs. Li/Li^+.[41–45] The VC-derived SEI layer effectively suppresses EC reduction at lower potentials, consistent with the reduced magnitude of the $dC_{C_2H_4}/dt$ profile shown in Fig. 7a.

The initial cathodic CV scan shows that both the onset and the position of the first reduction peak slightly shift towards a positive potential with a lower catalytic current (i.e., the reduction peak broadens), as compared to the cell using the VC-free electrolyte (Fig. 5a). The EIS spectra in Fig. 7b also notably altered, exhibiting a larger cell impedance with a higher
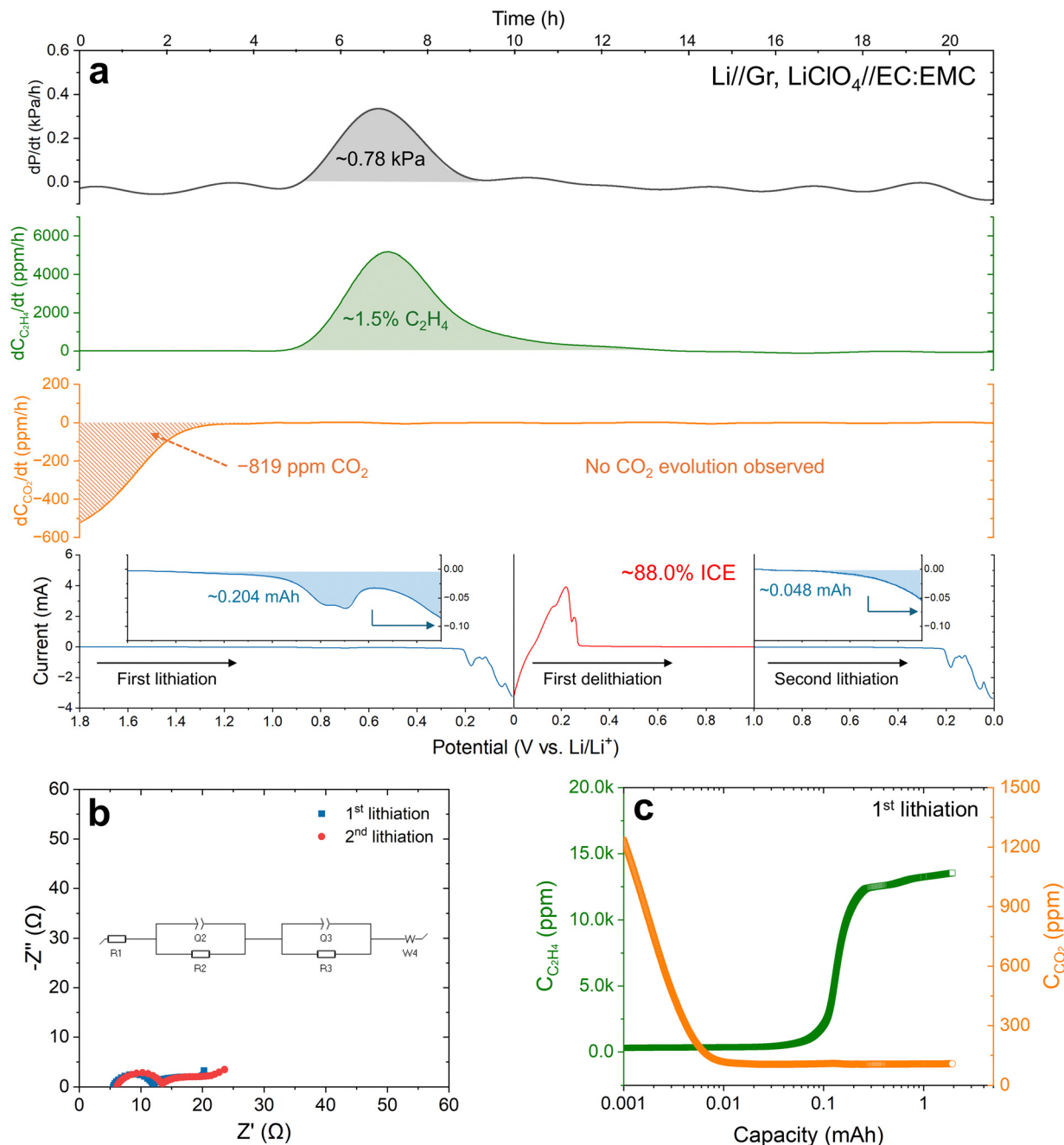
This journal is © The Royal Society of Chemistry 2025

Energy Environ. Sci., 2025, **18**, 8499–8514 | 8507

Fig. 6 *Operando* monitoring of gas evolution in the Li-graphite half-cell that undergoes cyclic voltammetry at a scan rate of 0.05 mV s^{-1} with 1 M LiClO$_4$ in EC : EMC 3 : 7 vol% as the electrolyte. (a) The obtained CV curves are plotted in conjunction with the change in concentrations of C$_2$H$_4$, CO$_2$, and in overall gas pressure. The detailed current variation from 1.8 V to 0.3 V *vs.* Li/Li$^+$ of the first lithiation and from 1 V to 0.3 V *vs.* Li/Li$^+$ of the second lithiation is provided in the insets by zooming in the *y*-axis. The blue shading of the first lithiation represents the electric charge consumed for the SEI formation and associated gas evolution. (b) The EIS spectra obtained after the initial and the second cathodic scan. (c) Evolution of C$_2$H$_4$ and CO$_2$ concentrations during the initial lithiation of graphite.

surface potential at ∼130 mV *vs.* Li/Li$^+$. Pritzl *et al.* conducted a quantitative study showing that a small addition of VC could lead to a higher impedance of the graphite anode, but (perhaps counterintuitively,) coupled with better cycling performance. Further addition of VC, however, can result in even higher impedances of both electrodes, leading to poorer cyclability.[42] Therefore, an optimal dosage of VC is required to grow a

reliable SEI layer that suppresses gas evolution, but without excessively increasing cell impedance.[41] In this regard, our gas sensing system can be an ideal tool to determine the optimal dosage of VC (or other electrolyte additives) through correlations between gas concentrations and cell impedances.

Generally, formation and consumption reactions of CO$_2$ can occur simultaneously at voltages below 1.5 V in LIB cells with
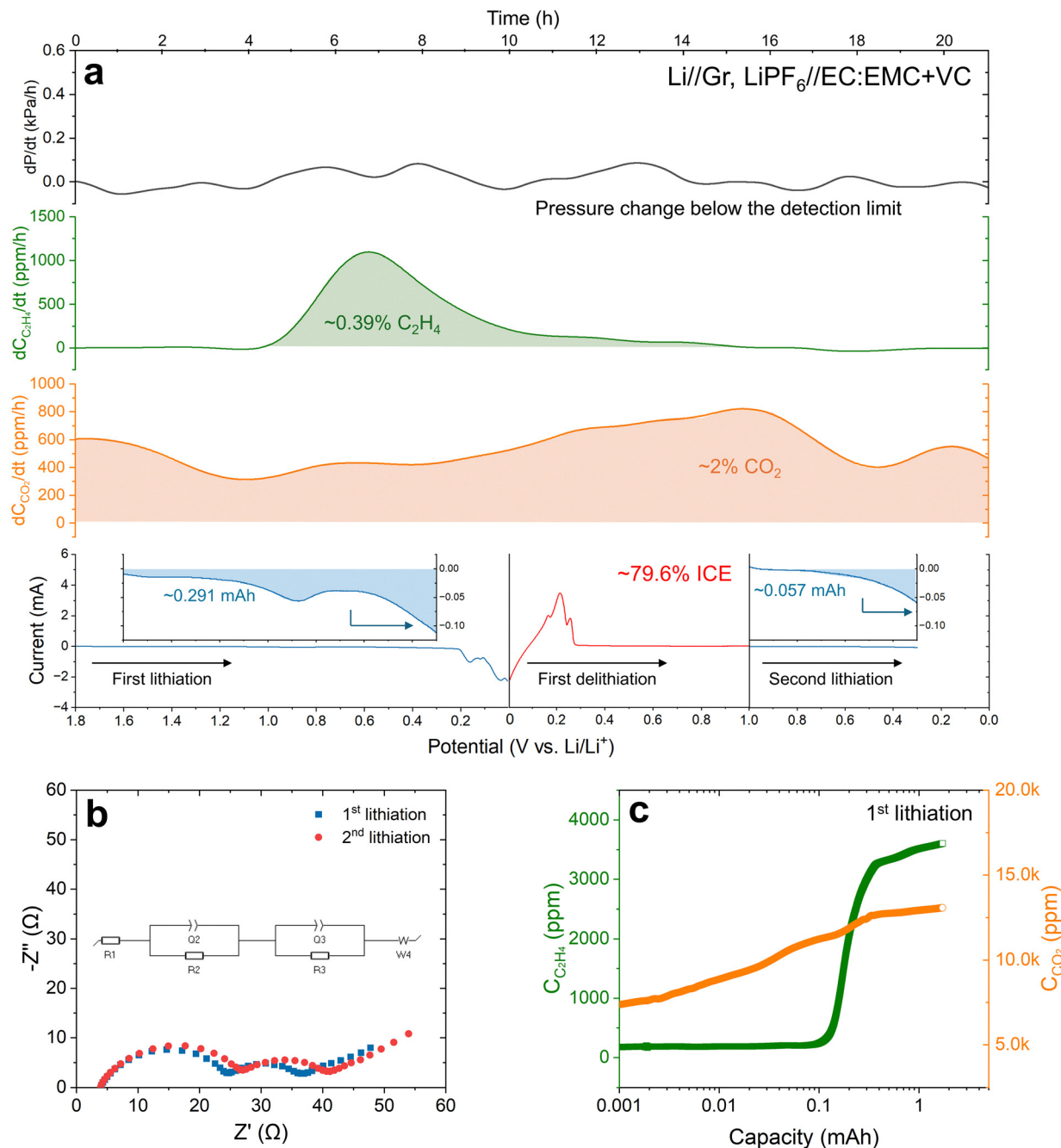
Fig. 7 *Operando* monitoring of gas evolution in the Li-graphite half-cell that undergoes cyclic voltammetry at a scan rate of 0.05 mV s^{-1} with 1 M LiPF$_6$ in EC : EMC 3 : 7 vol% + 2 vol% VC as the electrolyte. (a) The obtained CV curves are plotted in conjunction with the change in concentrations of C$_2$H$_4$, CO$_2$, and in overall gas pressure. The detailed current variation from 1.8 V to 0.3 V *vs.* Li/Li$^+$ of the first lithiation and from 1 V to 0.3 V *vs.* Li/Li$^+$ of the second lithiation is provided in the insets by zooming in the y-axis. The blue shading of the first lithiation represents the electric charge consumed for the SEI formation and associated gas evolution. (b) The EIS spectra obtained after the initial and the second cathodic scan. (c) Evolution of C$_2$H$_4$ and CO$_2$ concentrations during the initial lithiation of graphite.

common LiPF$_6$//carbonate electrolytes,[6] and the addition of VC further complicates the interpretation of the dC_{CO_2}/dt profile. In one study, VC reduction is reported to occur at a potential as high as *ca.* 1.9 V *vs.* Li/Li$^+$ and the generation of CO$_2$ involves VC ring-opening reactions driven by a nucleophilic attack that may be a spontaneous process.[30] Interestingly, as shown in Fig. 7c, the C$_2$H$_4$ signal also rises at ~0.1 mAh, like the observation in

Fig. 5c. This suggests that the additional generation of CO$_2$ caused by the presence of 2 vol% of VC does not seem to consume extra electrons before the onset of C$_2$H$_4$, supporting the hypothesis that it is driven by a chemical process rather than an electrochemical one. Despite this, a higher level of irreversible capacity, reflected in a poorer ICE of *ca.* 79.6%, is observed. This poorer ICE indicates that more electric charges

This journal is © The Royal Society of Chemistry 2025

Energy Environ. Sci., 2025, **18**, 8499–8514 | **8509**

are consumed in forming the VC-derived SEI layer rather than in generating CO_2 gas. Notably, VC is known to dominate SEI formation as long as it presents,[30] explaining why even a small addition of 2 vol% significantly impacts electrochemical signals, alters gassing behaviors, and leads to higher electrode impedances. These findings highlight the duality of VC, influencing both SEI formation and gas evolution dynamics.

Scalability of the technology for batteries and beyond

While selecting a homemade cell is to generate reliable data under controllable conditions and validate the newly developed HCF–PTS system for battery gas sensing, it is of equal importance to demonstrate the system's technological scalability for real-world applications. To do so, we demonstrate the use of our technology in monitoring the C_2H_4 and CO_2 dynamics in a commercial pouch Li-ion cell. The electrodes and electrolytes are identical to those presented in Fig. 4.

As presented in Fig. 8, the schematic illustrates how we enabled the attachment of our HCF–PTS sensor to the LFP-graphite pouch cell using a three-way valve (details can be found in Methods). Firstly, the soft pouch cell package swells evidently, leading to an unstable and dynamic internal pressure. The overall gas volume accumulated after the initial cycle was estimated to be ~ 3 ml using a syringe (Note 11, SI), which is at the same magnitude as that of the same type of $Li[Ni_{1/3}Mn_{1/3}Co_{1/3}]O_2$-graphite pouch cell determined by Archimedes' method.[40] The C_2H_4 profile exhibits the same onset point at a cell voltage of ~ 2.9 V, agreeing with that of the homemade cell. However, the C_2H_4 concentration increases gradually until reaching $\sim 8.2\%$ and $\sim 9.3\%$ after initial charge and discharge,

respectively. Importantly, given that the background CO_2 in the glovebox is only ~ 1500–2000 ppm, the spontaneous CO_2 formation is reflected by nearly 4% of CO_2 prior to charging the cell. As indicated by the orange arrow, a decline in CO_2 concentration coincides with the onset of C_2H_4 evolution. This decrease is suggested to be caused by the observed C_2H_4 evolution and the possible H_2 evolution reported elsewhere.[28] Afterward, the CO_2 concentration remains approximately at a constant level, as the C_2H_4 concentration climbs. A more pronounced increase in CO_2 concentration is observed during the discharge, accompanied by the stabilized C_2H_4 profile. Lastly, it should be noted that the gassing dynamics of a pouch cell are not directly comparable to that of our homemade cell due to the continuous change of overall gas pressure caused by cell swelling.

This demonstration clearly supports the potential of our sensing technology to be applied in commercial battery cells. For instance, our gas sensing technique (which detects gas concentration) and the Archimedes' method developed by Aiken *et al.* in 2014 (which measures gas volume)[46] may naturally form a great combination that leads to comprehensive analyses of gassing dynamics specifically for pouch cells. Applications for sensing other cell formats can be envisioned pending engineering efforts. Additionally, we have demonstrated a tailored water splitting experiment for *operando* monitoring of O_2 and CO_2 (detailed discussion in Note 12, SI), showcasing the substantial potential of our gas sensing technique for broader applications beyond the battery realm, particularly for aqueous-based electrochemical energy systems, such as aqueous batteries and electrolysis cells.
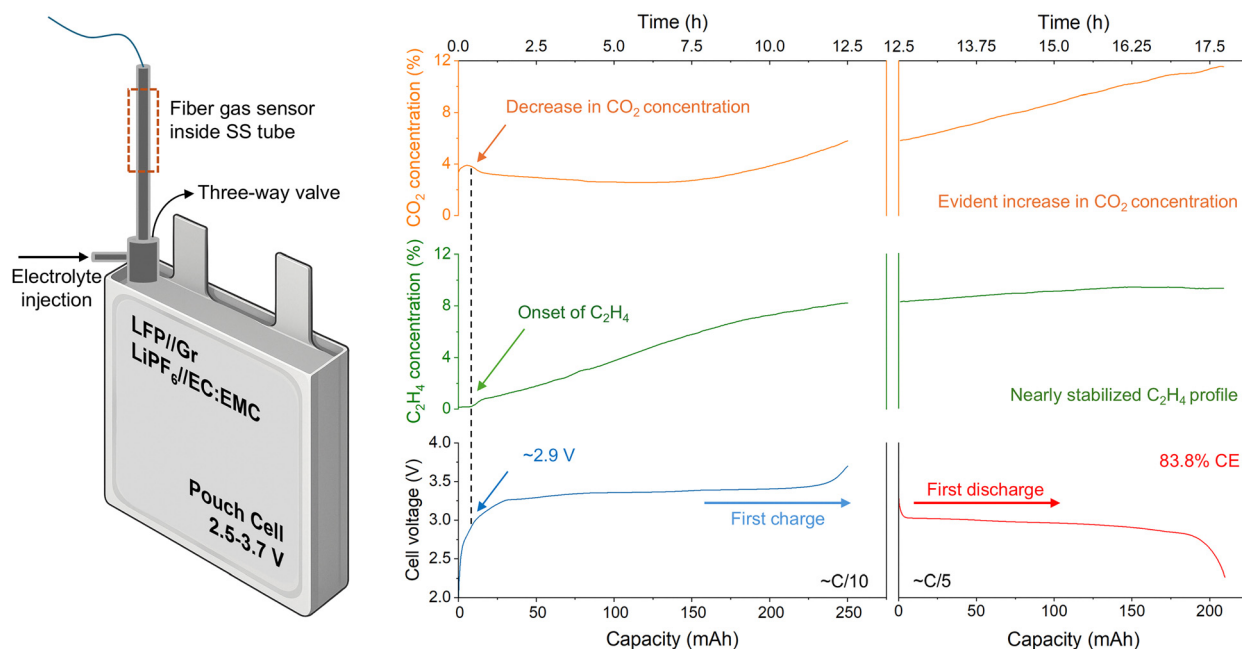

Fig. 8 *Operando* monitoring of gas evolution in a commercial $LiFePO_4$-Graphite pouch cell during the initial GCD cycle. A three-way valve was used to enable the attachment of HCF sensor and the electrolyte injection of 1 M $LiPF_6$ in EC : EMC 3 : 7 vol%. The same C-rates as the ones used in the homemade cell, *i.e.*, $\sim$C/10 (20 mA) and $\sim$C/5 (40 mA) were used for the initial charge and discharge, respectively. The digital image of such a pouch cell with an HCF sensor attached is provided in SI11.

8510 | *Energy Environ. Sci.*, 2025, **18**, 8499–8514

This journal is © The Royal Society of Chemistry 2025

Discussion

A novel gas sensing technique for characterizing battery cells based on HCF–PTS is presented. By embedding the HCF gas sensor directly into LIB cells, this approach enables real-time *operando* gas monitoring that resolves numerous challenges experienced in existing mass spectrometry-based technologies. In LIBs with EC-containing electrolytes, the SEI formation process generates C_2H_4 *via* reduction reactions, during which CO is also formed.[30] Measurement of C_2H_4 using DEMS/OEMS can be susceptible to the interference of CO, since they have the same *m/z* ratio of 28, thus complicating the reliable identification and quantification of gases.[9,47] In contrast, the proposed HCF–PTS is a spectroscopic technique for highly selective gas detection. Given that the selected pump lasers only interact with the target gas molecules near the absorption line center, the evolution of C_2H_4 can be selectively monitored without any interference from other gases like CO in LIB cells. Our technique therefore avoids complex post-data analyses, providing a straightforward way of selective gas monitoring with LODs of the ppm levels.

Moreover, measurements of gas evolution using DEMS/OEMS systems may disrupt the typical operating environment of an LIB cell due to their sampling-and-then-measuring approach by introducing a carrier gas flow, leading to possible data misinterpretations. In contrast, the miniature HCF sensor enables *operando* measurement and operates without the need for carrier gas, preserving the natural working conditions of LIB cells. Our approach enables the *operando* monitoring of gassing dynamics that more precisely reflects the (electro-)chemical reactions occurring within the LIB cells. Remarkably, our HCF–PTS gas sensing system has effectively identified spontaneous CO_2 formation immediately after the LIB cell assembly. Furthermore, our findings provide strong evidence that the PF_6 anions in electrolytes are the primary driver of this spontaneous CO_2 formation. By replacing $LiPF_6$ with $LiClO_4$ to deprive the intermediate gas components of PF_5 and POF_3, CO_2 formation was almost entirely suppressed. This spontaneous CO_2 formation becomes more pronounced when the $LiPF_6$-based electrolyte contains 2 vol% VC, emphasizing its significant impact on CO_2 evolution in LIB cells. In any case, such detailed observations are challenging to achieve with the DEMS/OEMS systems alone. As to whether CO_2 is problematic or not for near term or long-term cell reliability, it is beyond the scope of this work. But the first step in identifying a problem is to acknowledge that it exists, which is now possible with HCF–PTS.

Looking at the future technological roadmap, the HCF–PTS system can be conveniently upgraded for multi-component gas detection beyond C_2H_4 and CO_2. With the wide transmission window of the HCF, spanning from visible to mid-infrared range, multi-component gas detection inside LIBs is achievable. For example, by using additional pump lasers targeting the absorption lines of O_2 at 760 nm (Note 12, SI), H_2 at 2122 nm, CO at 4600 nm, and employing frequency- or time-division multiplexing techniques for signal separation, the system can detect simultaneously the five most common gas species during battery formation and operation, *i.e.*, C_2H_4, CO_2, H_2, CO, and O_2, providing a universal gas sensing solution for LIBs. The technique can also be readily extended to characterizing new materials in LIBs[48] and sensing sodium-ion batteries with similar cell design and chemistry.[49] From an engineering aspect, only the sensor head might degrade while the rest of the interrogation system remains unchanged. The cost of an HCF sensor head is typically in the range of several US dollars, which makes the sensor head financially competitive and replaceable for optimal performance during long-term operation.

The demonstrative experiment of sensing a commercial Li-ion pouch cell proves that our sensing method is readily adaptable for real-world applications, requiring only engineering efforts for sensor integration. In industries, our fiber sensing technology not only offers a promising real-time monitoring solution for rechargeable batteries during operation but also contributes to sustainability by enabling the evaluation of retired batteries, either for recycling or for extending their second life. By integrating the HCF–PTS sensing system with existing *operando* material characterization tools, such as electrochemical quartz-crystal microbalance (EQCM) and atomic force microscopy (AFM), the growth of SEI as well as the associated chemical reactions can be better understood. Similarly, the evolution of gases may be of critical importance to other applications such as electrocatalysis, artificial photosynthesis, and ammonia oxidation reactions, offering a wealth of possibilities for fiber-based sensing in electrochemical systems beyond batteries. Additionally, the proposed method has the potential to form synergistic combinations with existing gas sensing techniques, such as DEMS/OEMS, setting the stage for rich insights into the internal chemistry of various battery systems and beyond, particularly the field of electrochemical CO_2 reduction. While the reduction reactions convert CO_2 into various valuable products, whether CO_2 (C: +4) is reduced to form CO (C: +2), C_2H_4 (C: −2), or CH_4 (C: −4) remain largely unclear and uncontrollable. By implementing such an *operando* gas sensing method, 'electron-to-gas' pathways can be established for the given CO_2 reduction system, providing a scientific basis for further improvements in safety, reliability, and sustainability of future electrochemical energy systems.

Methods

Homemade cell assembly

Both half cells and full cells were assembled using the designated Li–air cell components purchased from MTI Corporation (HF-Kejing, China). The gas inlet and outlet were modified to adapt our optical fiber gas sensor and a commercial piezoelectric pressure sensor *via* Swagelok connectors (Note 1, SI). Li metal disks (400 μm thick) were bought from a local supplier (Liyuan Battery Ltd) in China. Graphite anode sheets (*ca.* 2.4 mAh cm^{-2}) were purchased from NEI Corporation (NJ, the US) and punched in 12-mm disks. $LiFePO_4$ cathode sheets (*ca.* 2.3 mAh cm^{-2}) were obtained from Li-Fun Technologies (Hunan Province, China) and punched in 16-mm disks. From

This journal is © The Royal Society of Chemistry 2025

Energy Environ. Sci., 2025, **18**, 8499–8514 | **8511**

their datasheets, the electrode thickness is calculated to be ~ 60 μm and ~ 67 μm, for the anode and the cathode, respectively. All these cell components were dried in a heating chamber at 100 °C under vacuum for at least 24 hours to achieve a sufficient drying process, prior to loading into an argon-filled glovebox ($H_2O \leq 0.5$ ppm; $O_2 \leq 0.5$ ppm). Given that CO_2 is not controlled in the glovebox, its concentration was determined to be between 1500 ppm and 2000 ppm using a commercial electrochemical sensor. For the separator made of glass fibers (Whatman®), however, the drying temperature and time was raised to 150 °C and 48 hours, respectively, to largely remove all residue moisture. The three electrolyte blends were freshly made upon request by DoDoChem (China) with limited water contents (≤ 10 ppm). The volume of the liquid electrolyte is precisely controlled by a high-precision pipette to be 200 μL for each practice.

Li-ion pouch cell construction

Commercially available Li-ion dry pouch cells were obtained from Li-Fun Technologies (Hunan Province, China). According to the datasheet provided by the supplier, the nominal capacity of such an LFP-graphite cell is 200 mAh with mass loadings of 16 mg cm^{-2} LFP and 7.7 mg cm^{-2} graphite. A three-way stopcock valve and a 5 mL medical syringe were connected to the pouch cell to accommodate the optical fiber sensor and to regulate internal gas pressure during the test. Prior to filling with 1.5 mL LP57 liquid electrolyte, the cells were open and dried inside a vacuum oven at 70 °C for more than 48 hours. The cell was instantly transferred into the glovebox under vacuum.

Electrochemical measurements

The electrochemical performances of the homemade cell were evaluated by cyclic voltammetry (CV) for half cells and galvanostatic charge–discharge (GCD) for full cells using a Vertex. One potentiostat (Ivium Technologies, the Netherlands). Electrochemical impedance spectroscopy (EIS) of coin cells was done using a VMP Potentiostat (BioLogic, France). The homemade cell was placed into a temperature chamber (ESCO Lifesciences Group) held at 35 °C prior to each electrochemical test. For CV of half cells, a scan rate of 0.05 mV s^{-1} (relatively slow to that used in other studies) is selected to isolate individual activities at different potentials $vs.$ Li/Li$^+$. The open circuit voltage is first brought down to 5 mV $vs.$ Li/Li$^+$, and then the cycling was between 5 mV and 1 V $vs.$ Li/Li$^+$. For GCD of full homemade cells, a rate of $\sim$C/10 ($i.e.$, ~ 0.2 mA cm^{-2}-LFP) is used for the initial charging process to largely allow a complete formation of solid–electrolyte interphase (SEI). The C-rate is then adjusted to $\sim$C/5 ($i.e.$, ~ 0.4 mA cm^{-2}-LFP) for the first discharge and the subsequent cycle with a voltage window of 2.7–3.7 V.

Author contributions

W. J., T. Z., H. B., and S. T. B. conceived the idea of $operando$ battery gas sensing using HCF–PTS. T. Z., H. B., S. T. B., and

F. C. designed the experiments, and T. Z., H. B., and F. C. built the systems and conducted the experiments. J. W. and H. L. H. assisted in building the systems and conducting the experiments. T. Z., H. B., F. C., J. W., and W. J. analyzed the results and prepared the manuscript. J. W. and P. Z. assisted with the data analysis. S. G. and Y. W. designed and fabricated the HCF. J. H., L. Z., and S. T. B. discussed the results, edited and proofread the manuscript. W. J. and H. B. coordinated the project.

Conflicts of interest

The authors declare no competing interests.

Data availability

The datasets of this study are available in the article and its SI. Raw data will be made available from the corresponding author upon reasonable request.

Supplementary information is available: Supplementary Note 1–12; Fig. S1–S16. See DOI: https://doi.org/10.1039/d5ee04211a

Acknowledgements

References

1 Z. J. Baum, R. E. Bird, X. Yu and J. Ma, Lithium-Ion Battery Recycling – Overview of Techniques and Trends, *ACS Energy Lett.*, 2022, 7(2), 712–719.

2 J. Huang, S. T. Boles and J.-M. Tarascon, Sensing as the key to battery lifetime and sustainability, *Nat. Sustainability*, 2022, 5(3), 194–204.

3 X. Lu, J.-M. Tarascon and J. Huang, Perspective on commercializing smart sensing for batteries, *eTransportation*, 2022, **14**, 100207.

4 B. S. Parimalam, A. D. MacIntosh, R. Kadam and B. L. Lucht, Decomposition Reactions of Anode Solid Electrolyte Interphase (SEI) Components with LiPF$_6$, *J. Phys. Chem. C*, 2017, **121**(41), 22733–22738.

5 W. Mei, Z. Liu, C. Wang, C. Wu, Y. Liu, P. Liu, X. Xia, X. Xue, X. Han, J. Sun and G. Xiao, H.-y. Tam, J. Albert, Q. Wang, T.

8512 | *Energy Environ. Sci.*, 2025, **18**, 8499–8514

This journal is © The Royal Society of Chemistry 2025

Guo, *Operando* monitoring of thermal runaway in commercial lithium-ion cells via advanced lab-on-fiber technologies, *Nat. Commun.*, 2023, **14**(1), 5251.

6 R. Lundström, N. Gogoi, X. Hou and E. J. Berg, Competing Ethylene Carbonate Reactions on Carbon Electrode in Li-Ion Batteries, *J. Electrochem. Soc.*, 2023, **170**(4), 040516.

7 S. Solchenbach, M. Metzger, M. Egawa, H. Beyer and H. A. Gasteiger, Quantification of PF_5 and POF_3 from Side Reactions of $LiPF_6$ in Li-Ion Batteries, *J. Electrochem. Soc.*, 2018, **165**(13), A3022.

8 B. Michalak, B. B. Berkes, H. Sommer, T. Bergfeldt, T. Brezesinski and J. Janek, Gas Evolution in $LiNi_{0.5}Mn_{1.5}O_4$/Graphite Cells Studied In *Operando* by a Combination of Differential Electrochemical Mass Spectrometry, Neutron Imaging, and Pressure Measurements, *Anal. Chem.*, 2016, **88**(5), 2877–2883.

9 B. Strehle, S. Solchenbach, M. Metzger, K. U. Schwenke and H. A. Gasteiger, The Effect of CO_2 on Alkyl Carbonate Trans-Esterification during Formation of Graphite Electrodes in Li-Ion Batteries, *J. Electrochem. Soc.*, 2017, **164**(12), A2513–A2526.

10 L. Zhang, C. Tsolakidou, S. Mariyappan, J.-M. Tarascon and S. Trabesinger, Unraveling gas evolution in sodium batteries by online electrochemical mass spectrometry, *Energy Storage Mater.*, 2021, **42**, 12–21.

11 J. Huang, L. Albero Blanquer, J. Bonefacino, E. R. Logan, D. Alves Dalla Corte, C. Delacourt, B. M. Gallant, S. T. Boles, J. R. Dahn, H.-Y. Tam and J.-M. Tarascon, *Operando* decoding of chemical and thermal events in commercial Na(Li)-ion cells via optical sensors, *Nat. Energy*, 2020, **5**(9), 674–683.

12 J. Huang, X. Han, F. Liu, C. Gervillié, L. A. Blanquer, T. Guo and J.-M. Tarascon, Monitoring battery electrolyte chemistry via in-*operando* tilted fiber Bragg grating sensors, *Energy Environ. Sci.*, 2021, **14**(12), 6464–6475.

13 C. Gervillié-Mouravieff, C. Boussard-Plédel, J. Huang, C. Leau, L. A. Blanquer, M. B. Yahia, M. L. Doublet, S. T. Boles, X. H. Zhang, J. L. Adam and J. M. Tarascon, Unlocking cell chemistry evolution with *operando* fibre optic infra-red spectroscopy in commercial Na(Li)-ion batteries, *Nat. Energy*, 2022, **7**(12), 1157–1169.

14 P. Zhao, Y. Zhao, H. Bao, H. L. Ho, W. Jin, S. Fan, S. Gao, Y. Wang and P. Wang, Mode-phase-difference photothermal spectroscopy for gas detection with an anti-resonant hollow-core optical fiber, *Nat. Commun.*, 2020, **11**(1), 847.

15 W. Jin, Y. Cao, F. Yang and H. L. Ho, Ultra-sensitive all-fibre photothermal spectroscopy with large dynamic range, *Nat. Commun.*, 2015, **6**(1), 6767.

16 Y. Lin, W. Jin, F. Yang, Y. Tan and H. L. Ho, Performance optimization of hollow-core fiber photothermal gas sensors, *Opt. Lett.*, 2017, **42**(22), 4712–4715.

17 S. W. Sharpe, T. J. Johnson, R. L. Sams, P. M. Chu, G. C. Rhoderick and P. A. Johnson, Gas-Phase Databases for Quantitative Infrared Spectroscopy, *Appl. Spectrosc.*, 2004, **58**(12), 1452–1461.

18 I. E. Gordon, L. S. Rothman, R. J. Hargreaves, R. Hashemi, E. V. Karlovets and F. M. Skinner, *et al.*, The HITRAN2020 molecular spectroscopic database, *J. Quant. Spectrosc. Radiat. Transfer*, 2022, **277**, 107949.

19 T. Zheng, M. Muneeswara, H. Bao, J. Huang, L. Zhang, D. S. Hall, S. T. Boles and W. Jin, Gas Evolution in Li-Ion Rechargeable Batteries: A Review on *Operando* Sensing Technologies, Gassing Mechanisms, and Emerging Trends, *ChemElectroChem*, 2024, **11**(15), e202400065.

20 F. Liu, H. Bao, H. L. Ho, W. Jin, S. Gao and Y. Wang, Multicomponent trace gas detection with hollow-core fiber photothermal interferometry and time-division multiplexing, *Opt. Express*, 2021, **29**(26), 43445–43453.

21 F. Chen, S. Jiang, W. Jin, H. Bao, H. L. Ho, C. Wang and S. Gao, Ethane detection with mid-infrared hollow-core fiber photothermal spectroscopy, *Opt. Express*, 2020, **28**(25), 38115–38126.

22 F. Chen, S. Jiang, H. L. Ho, S. Gao, Y. Wang and W. Jin, Frequency-Division-Multiplexed Multicomponent Gas Sensing with Photothermal Spectroscopy and a Single NIR/MIR Fiber-Optic Gas Cell, *Anal. Chem.*, 2022, **94**(39), 13473–13480.

23 S. E. Bialkowski, N. G. C. Astrath and M. A. Proskurnin, Photothermal Spectroscopy in Homogeneous Samples, *Photothermal Spectroscopy Methods*, 2019, ch. 5, pp. 219–284.

24 M. Onuki, S. Kinoshita, Y. Sakata, M. Yanagidate, Y. Otake, M. Ue and M. Deguchi, Identification of the Source of Evolved Gas in Li-Ion Batteries Using #2#1 -labeled Solvents, *J. Electrochem. Soc.*, 2008, **155**(11), A794.

25 S. K. Heiskanen, J. Kim and B. L. Lucht, Generation and Evolution of the Solid Electrolyte Interphase of Lithium-Ion Batteries, *Joule*, 2019, **3**(10), 2322–2333.

26 M. Metzger, B. Strehle, S. Solchenbach and H. A. Gasteiger, Origin of H_2 Evolution in LIBs: H_2O Reduction vs. Electrolyte Oxidation, *J. Electrochem. Soc.*, 2016, **163**(5), A798–A809.

27 R. Bernhard, M. Metzger and H. A. Gasteiger, Gas Evolution at Graphite Anodes Depending on Electrolyte Water Content and SEI Quality Studied by On-Line Electrochemical Mass Spectrometry, *J. Electrochem. Soc.*, 2015, **162**(10), A1984–A1989.

28 L. D. Ellis, J. P. Allen, L. M. Thompson, J. E. Harlow, W. J. Stone, I. G. Hill and J. R. Dahn, Quantifying, Understanding and Evaluating the Effects of Gas Consumption in Lithium-Ion Cells, *J. Electrochem. Soc.*, 2017, **164**(14), A3518.

29 M. Metzger, C. Marino, J. Sicklinger, D. Haering and H. A. Gasteiger, Anodic oxidation of conductive carbon and ethylene carbonate in high-voltage Li-ion batteries quantified by on-line electrochemical mass spectrometry, *J. Electrochem. Soc.*, 2015, **162**(7), A1123.

30 R. Lundström, N. Gogoi, T. Melin and E. J. Berg, Unveiling Reaction Pathways of Ethylene Carbonate and Vinylene Carbonate in Li-Ion Batteries, *J. Phys. Chem. C*, 2024, **128**(20), 8147–8153.

31 T. Zheng, D. Kramer, M. H. Tahmasebi, R. Mönig and S. T. Boles, Exploring the Reversibility of Phase Transformations in Aluminum Anodes through *Operando* Light

This journal is © The Royal Society of Chemistry 2025

Energy Environ. Sci., 2025, **18**, 8499–8514 | 8513

Microscopy and Stress Analysis, *ChemSusChem*, 2020, **13**(22), 5910–5920.

32 C. G. Barlowz, Reaction of Water with Hexafluorophosphates and with Li Bis(perfluoroethylsulfonyl)imide Salt, *Electrochem. Solid-State Lett.*, 1999, **2**(8), 362.

33 J. Lamb, C. J. Orendorff, E. P. Roth and J. Langendorf, Studies on the Thermal Breakdown of Common Li-Ion Battery Electrolyte Components, *J. Electrochem. Soc.*, 2015, **162**(10), A2131.

34 S. E. Sloop, J. K. Pugh, S. Wang, J. B. Kerr and K. Kinoshita, Chemical Reactivity of PF_5 and $LiPF_6$ in Ethylene Carbonate/Dimethyl Carbonate Solutions, *Electrochem. Solid-State Lett.*, 2001, **4**(4), A42.

35 S. E. Sloop, J. B. Kerr and K. Kinoshita, The role of Li-ion battery electrolyte reactivity in performance decline and self-discharge, *J. Power Sources*, 2003, **119–121**, 330–337.

36 B. Ravdel, K. M. Abraham, R. Gitzendanner, J. DiCarlo, B. Lucht and C. Campion, Thermal stability of lithium-ion battery electrolytes, *J. Power Sources*, 2003, **119–121**, 805–810.

37 C. L. Campion, W. Li and B. L. Lucht, Thermal Decomposition of $LiPF_6$-Based Electrolytes for Lithium-Ion Batteries, *J. Electrochem. Soc.*, 2005, **152**(12), A2327.

38 M. Holzapfel, A. Würsig, W. Scheifele, J. Vetter and P. Novák, Oxygen, hydrogen, ethylene and CO_2 development in lithium-ion batteries, *J. Power Sources*, 2007, **174**(2), 1156–1160.

39 L. Xing, W. Li, C. Wang, F. Gu, M. Xu, C. Tan and J. Yi, Theoretical Investigations on Oxidative Stability of Solvents and Oxidative Decomposition Mechanism of Ethylene Carbonate for Lithium Ion Battery Use, *J. Phys. Chem. B*, 2009, **113**(52), 16596–16602.

40 C. P. Aiken, J. Self, R. Petibon, X. Xia, J. M. Paulsen and J. R. Dahn, A Survey of In Situ Gas Evolution during High Voltage Formation in Li-Ion Pouch Cells, *J. Electrochem. Soc.*, 2015, **162**(4), A760.

41 K. U. Schwenke, S. Solchenbach, J. Demeaux, B. L. Lucht and H. A. Gasteiger, The Impact of CO_2 Evolved from VC and FEC during Formation of Graphite Anodes in Lithium-Ion Batteries, *J. Electrochem. Soc.*, 2019, **166**(10), A2035.

42 D. Pritzl, S. Solchenbach, M. Wetjen and H. A. Gasteiger, Analysis of Vinylene Carbonate (VC) as Additive in Graphite/$LiNi_{0.5}Mn_{1.5}O_4$ Cells, *J. Electrochem. Soc.*, 2017, **164**(12), A2625.

43 H. Ota, Y. Sakata, A. Inoue and S. Yamaguchi, Analysis of Vinylene Carbonate Derived SEI Layers on Graphite Anode, *J. Electrochem. Soc.*, 2004, **151**(10), A1659.

44 S. Grugeon, P. Jankowski, D. Cailleu, C. Forestier, L. Sannier, M. Armand, P. Johansson and S. Laruelle, Towards a better understanding of vinylene carbonate derived SEI-layers by synthesis of reduction compounds, *J. Power Sources*, 2019, **427**, 77–84.

45 P. G. Kitz, M. J. Lacey, P. Novák and E. J. Berg, *Operando* investigation of the solid electrolyte interphase mechanical and transport properties formed from vinylene carbonate and fluoroethylene carbonate, *J. Power Sources*, 2020, **477**, 228567.

46 C. P. Aiken, J. Xia, D. Y. Wang, D. A. Stevens, S. Trussler and J. R. Dahn, An Apparatus for the Study of In Situ Gas Evolution in Li-Ion Pouch Cells, *J. Electrochem. Soc.*, 2014, **161**(10), A1548.

47 B. B. Berkes, A. Jozwiuk, M. Vračar, H. Sommer, T. Brezesinski and J. Janek, Online Continuous Flow Differential Electrochemical Mass Spectrometry with a Realistic Battery Setup for High-Precision, Long-Term Cycling Tests, *Anal. Chem.*, 2015, **87**(12), 5878–5883.

48 T. Zheng and S. T. Boles, Lithium aluminum alloy anodes in Li-ion rechargeable batteries: past developments, recent progress, and future prospects, *Prog. Energy*, 2023, **5**(3), 032001.

49 J. Zhang and T. Zheng, Group IVA Alloy Anodes for Sodium-Ion Rechargeable Batteries: Electrochemistry, Mechanics, and Kinetics, *Batteries Supercaps*, 2025, e202400823.

8514 | *Energy Environ. Sci.*, 2025, **18**, 8499–8514

This journal is © The Royal Society of Chemistry 2025